applied sciences

MDPI

Article

Generation of High-Density Pulsed Gas–Liquid Discharge Plasma Using Floating Electrode Configuration at Atmospheric Pressure

Shuqi Li [1,2], Yunhu Liu [1,2,*], Hao Yuan [3], Jianping Liang [3], Min Zhang [1,2], Yao Li [3] and Dezheng Yang [2,3,*]

[1] School of Sciences, Shihezi University, Shihezi 832003, China
[2] Key Laboratory of Environmental Monitoring and Pollutant Control of Xinjiang Bingtuan, Shihezi University, Shihezi 832003, China
[3] Key Laboratory of Materials Modification by Laser, Ion, and Electron Beams, Ministry of Education, Dalian University of Technology, Dalian 116024, China
* Correspondence: liuyh@shzu.edu.cn (Y.L.); yangdz@dlut.edu.cn (D.Y.)

Abstract: In this paper, a high-density gas–liquid discharge plasma is obtained combined with nanosecond pulse voltage and a floating electrode. The discharge images, the waveforms of pulse voltage and discharge current, and the optical emission spectra are recorded. Gas temperature and electron density are calculated by the optical emission spectra of N_2 ($C^3\Pi_u \rightarrow B^3\Pi_g$) and the Stark broadening of H_α, respectively. The emission intensities of N_2 ($C^3\Pi_u \rightarrow B^3\Pi_g$), N_2^+ ($B^2\Sigma \rightarrow X^2\Pi$), OH ($A^2\Sigma \rightarrow X^2\Pi$), O ($3p^5P \rightarrow 3s^5S^0$), He ($3d^3D \rightarrow 3p^3P_2^0$), gas temperature, and electron density are acquired by optical emission spectra to discuss plasma characteristics varying with spatial distribution, discharge gap, and gas flow rate. The spatial distributions of discharge characteristics, including gas temperature, electron density, and emission intensities of N_2 ($C^3\Pi_u \rightarrow B^3\Pi_g$), N_2^+ ($B^2\Sigma \rightarrow X^2\Pi$), OH ($A^2\Sigma \rightarrow X^2\Pi$), O ($3p^5P \rightarrow 3s^5S^0$), and He ($3d^3D \rightarrow 3p^3P_2^0$), are presented. It is found that a high-density discharge plasma with the electron density of 2.2×10^{15} cm^{-3} and low gas temperature close to room temperature is generated. While setting the discharge gap distance at 10 mm, the discharge area over liquid surface has the largest diameter of 20 mm; under the same conditions, electron density is in the order of 10^{15} cm^{-3}, and gas temperature is approximately 330 K. In addition, the discharge plasma characteristics are not kept consistent in the axial direction, in which the emission intensities of N_2^+ ($B^2\Sigma \rightarrow X^2\Pi$), N_2 ($C^3\Pi_u \rightarrow B^3\Pi_g$), OH ($A^2\Sigma \rightarrow X^2\Pi$), and gas temperature increased near the liquid surface. As the discharge gap is enlarged, the gas temperature increases, whereas the electron density remains almost constant. Moreover, as the gas flow rate was turned up, the electron density increased and the gas temperature was kept constant at 320 K.

Keywords: gas–liquid discharge; optical emission spectra; electron density; gas temperature

Citation: Li, S.; Liu, Y.; Yuan, H.; Liang, J.; Zhang, M.; Li, Y.; Yang, D. Generation of High-Density Pulsed Gas–Liquid Discharge Plasma Using Floating Electrode Configuration at Atmospheric Pressure. *Appl. Sci.* **2022**, *12*, 8895. https://doi.org/10.3390/app12178895

Academic Editor: Dawei Liu

Received: 29 July 2022
Accepted: 1 September 2022
Published: 5 September 2022

1. Introduction

Atmospheric pressure (AP) gas–liquid discharge plasma has been actively investigated for its promising application prospects in water purification [1–3], biomedicine [4–6], and materials processing [7–9]. However, random micro discharge channels occur easily which can lead to non-directed energy distribution leading to serious issues and adversely affecting industrial applications. Hence a stable gas–liquid discharge at AP is expected. Over the last two decades, various factors have been studied for improving discharge stability, including the electrode structures [10,11], the driving power supply [12,13], the working gases characteristic [14,15], and many other experimental parameters. In addition, the plasma characteristic could be different even under the same conditions [16], because it is influenced by electron transport. Thus, it is necessary to discuss the mechanism that leads to the change of the discharge mode, such as the glow to arc transition (GAT), which is a common result of thermal and electronic instability. Both of those instabilities are intensified by positive feedback via Joule heating [17]; more specifically, a slight increase in temperature can lead to a significant increase in vibrational–translational relaxation

rate, which improves gas temperature further via their exponential relationship [18]. In addition, the heat release happens in a small volume that allows thermal instability to develop rapidly.

Nanosecond pulse voltage can be used to generate stable non-thermal plasma, where the fast-rising time can prevent the GAT effectively. Since the rising time of nanosecond pulse voltage is shorter than the character time of gas heating (in microsecond scale) [19], the increase in gas temperature is not obvious. When the pulse voltage is applied, the rapidly rising voltage pulse induces a high electric field, which promotes the occurrence of non-equilibrium plasma [20], and the electrical energy delivered in the plasma discharge is mainly deposited in the energetic electrons instead of heating the heavy particles. Therefore, the nanosecond pulse voltage can be employed to generate a stable gas–liquid discharge with high electron density and low gas temperature [21,22]. Herrmann et al. [23] studied the influences of peak voltage and discharge gap distance on pulsed discharge behavior over the liquid surface. Gromov et al. [24] reported the physical process at the gas–liquid interface in a single pulse mode and high-frequency burst. Xu et al. [25] compared the pulsed discharge plasma and sinusoidal discharge plasma, the results showing that nanosecond pulsed discharge plasma has lower gas temperature and higher efficiency of bacterial inactivation in liquid than that of the sinusoidal discharge plasma. Wang et al. [26] used bipolar nanosecond pulse power to obtain a gas–liquid discharge plasma with electron density in the order of 10^{15} cm^{-3} and gas temperature of 350 K. They studied it further and reported in [27] that the electron density can be elevated to the order of 10^{17} cm^{-3} for the transient to spark discharge, with a gas temperature of 380 K.

In addition, the floating electrode (FE), as a kind of independent structure between electrodes, shows the potential to improve the discharge plasma characteristics [28,29]. As Hu et al. [30] reported, the FE can influence the place of initial current density increase. Lee et al. [31] compared electric field intensity distributions in a plasma jet with and without the inner-FE. The results show that the removal of FE improves plasma reactivity and lowers gas breakdown voltage. Liu et al. [32] developed a diffuse-like discharge and studied the spatial electric field distribution when the FE is set. The report shows that the spatial electric field near the FE is advantageous for generating uniform-density plasma. But there are few studies on the gas–liquid discharge when FE is employed.

In this paper, with the employment of bipolar nanosecond pulse voltage, a kind of new electrode structure is used to attempt to obtain a stable discharge over the liquid surface. The electron structure is composed of a floating electrode and a hollow high voltage electron. A series of studies on the floating electrode gas–liquid discharge (FEGLD) is presented in this paper, including discharge images, electrical characteristics, optical emission spectra, plasma gas temperatures, and electron density. The spatial distribution characteristics of FEGLD are also carried out. Moreover, the interaction area between high density and low gas temperature at AP is expected to be enlarged by adjusting the discharge operation conditions. The influence on FEGLD by the discharge gap distance and gas flow rate is described in detail.

2. Experiment Setup

Figure 1a illustrates the experiment setup of FEGLD, comprising a discharge reactor, a nanosecond pulse power supply, the electrical characterization measurement system, and the optical emission spectra (OES) detection system. He (99.999%) is used as work gas. Figure 1b shows the diagram of the discharge reactor in which a stainless-steel hollow electrode inserts into PTFE. The floating electrode is fixed 2 mm below the end of the high voltage electrode. The bipolar nanosecond pulse power supply (DGM-40, 100 MHz, Dalian Power Supply Technology Co., Ltd., Dalian, China) provides pulse peak voltage which is adjustable in the range of 0–60 kV. A high voltage probe (Tektronix P6015A 1000×, 3.0 pF, 100 MΩ) and a current probe (Tektronix TCP312, bandwidth 100 MHz) are used to measure pulse voltage and discharge current, which are displayed on the oscilloscope (Tektronix, TDS5054B, 500 MHz). These compose the electrical characterization measurement system.

The optical fiber and grating monochromator (Andor SR750i) are employed as the OES detection system.

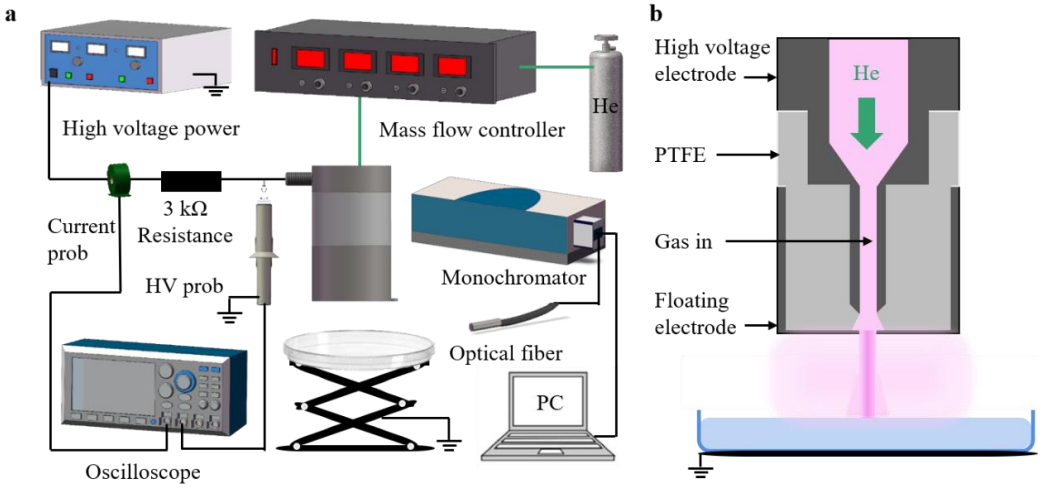

Figure 1. Experiment setup of FEGLD plasma with (**a**) experiment schematic and (**b**) discharge reactor diagram.

3. Result and Discussion

3.1. Visualization Characteristics of FEGLD Plasma

Since the plasma and liquid surface interaction area could be varied by changing the discharge gap, Figure 2 shows the discharge images of FEGLD at the discharge gap of 10 mm, 13 mm, and 15 mm, captured by a Canon 550D digital camera with 500 ms exposure time, under the measurement conditions of 3.5 L/min gas flow rate and 30 kV pulse peak voltage. As Figure 2 shows, when the discharge gap is set at 10 mm, there is a discharge area over the liquid surface with the diameter larger than 20 mm, and no flames or unstable discharge model transition can be observed. In the middle of this, a mean discharge area has the most intense emission intensity. While enlarging the discharge gap distance from 10 mm to 15 mm, as shown in the figure, there is an obvious contraction in the discharge area over the liquid surface.

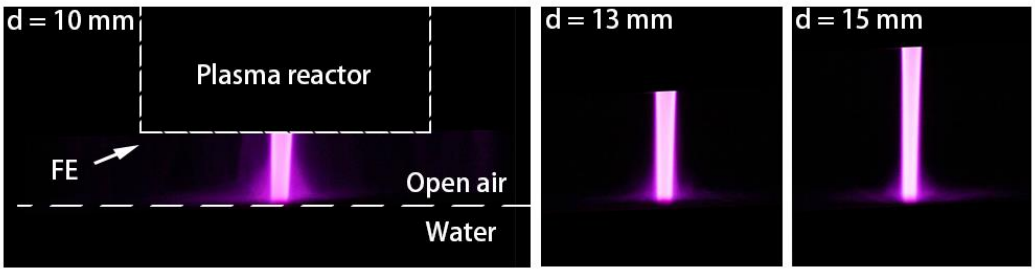

Figure 2. Discharge images of FEGLD plasma with variations in the discharge gap.

3.2. Spectral Characteristics of FEGLD

The OES emitted from the FEGLD are illustrated in Figure 3, under the experimental conditions of 30 kV pulse peak voltage, 12 mm discharge gap, and 3.5 L/min gas flow rate. The OES of FEGLD is mainly composed of the second positive system of N_2 ($C^3\Pi_u \rightarrow B^3\Pi_g$), the first negative system N_2^+ ($B^2\Sigma_u^+ \rightarrow X^2\Sigma_g^+$), the bands of OH ($A^2\Sigma \rightarrow X^2\Pi$), and the lines of He, H_α and O. The FEGLD is operated into open air filled with N_2, O_2, and H_2O originating in liquid surface. In He discharge, the metastable helium is easily quenched by those molecules. These processes are shown as R(1)–R(3) in Table 1. While the pulse voltage is employed, the production of electrons via Penning ionization sustains the plasma between two discharge pulses [14]. The N_2 (C) state could be produced by the ground

state of nitrogen molecules N_2 (X), as shown in R(4)–R(5). It should be mentioned that R(5) could release additional energy [18] contributing to temperature improvement as the gas fast heating mechanism. The first negative system N_2^+ ($B^2\Sigma_u^+ \rightarrow X^2\Sigma_g^+$) in FEGLD exhibited high emission intensity, as shown in Figure 3, the physicochemical process being shown in R6. Besides, the non-elastic collisions of the energetic electrons with N_2, O_2, and H_2O molecules will induce its dissociation, excitation, and ionization [33]. The process of energetic electrons created by the discharge pulse colliding with O_2 [34] is shown in R7. The physicochemical process of OH generation is shown in R8. Meanwhile, when the surrounding gas contains O_2 and H_2O, the collisional quenching of OH (A) by O_2 is an important process, as shown in R9.

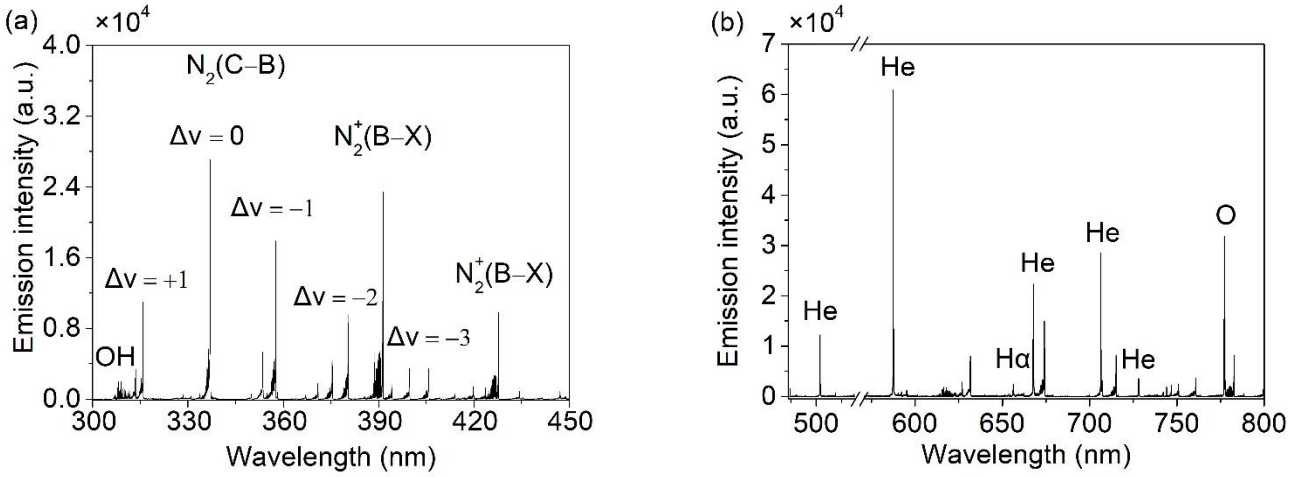

Figure 3. Typical optical emission spectrum generated by FEGLD plasma in the wavelength range of (**a**) 300–450 nm and (**b**) 450–800 nm.

Table 1. Related reactions for active species in FEGLD.

NO.	Reaction	Rate Constant	Ref.
1	$He^* + N_2 \rightarrow N_2^+ + He + e$	7.0×10^{-11} cm^3 s^{-1}	[35]
2	$He^* + O_2 \rightarrow O_2^+ + He + e$	2.6×10^{-16} cm^3 s^{-1}	[36]
3	$He^* + H_2O \rightarrow He + OH^+ + H^+ + e$	1.5×10^{-10} cm^3 s^{-1}	[37]
4	$e + N_2(X) \rightarrow e + N_2(A)$	1.1×10^{-10} cm^3 s^{-1}	[33]
5	$N_2(A) + N_2(A) \rightarrow N_2(C) + N_2(X)$	8.0×10^{-11} cm^3 s^{-1}	[33]
6	$e + N_2(A) \rightarrow 2e + N_2^+$	2.4×10^{-12} cm^3 s^{-1}	[34]
7	$e + O_2 \rightarrow e + O + O$	3.2×10^{-11} cm^3 s^{-1}	[34]
8	$e + H_2O \rightarrow e + H + OH$	2.6×10^{-12} cm^3 s^{-1}	[34]
9	$OH(A) + O_2(X) \rightarrow HO_2(X) + O(^3P)$	——	[38]

* Metastable state.

3.3. Electrical Characteristics of FEGLD

The distinction in discharge characteristics can be observed at pulse voltage duration times of positive and negative. Hence, the waveforms of the discharge current and topical voltage in positive pulse voltage and negative pulse voltage are presented in Figure 4a,b, under the experimental condition of 12 mm discharge gap, 30 kV pulse peak voltage, and 3.5 L/min gas flow rate. Figure 4a shows that the discharges mainly occur at the rising edge of positive pulse voltage, which has the rising time of about 250 ns. When the gas is broken down, one discharge current peak with 1.5 µs pulse width can be observed. In addition, three burr-like current peaks appear at the rising edge of the main discharge current peak. Each of those burr-like current peaks has the width of 50 ns. The characteristic of discharge current waveforms in negative pulse voltage is similar to that in positive pulse voltage, except their opposite polarity. In addition, there are a number of oscillations and a long plateau for voltage in each pulse. It is due to the power supply and capacitive loads in

FEGLD that the charge accumulation at the plasma–liquid interface reduced the space charge loss, and sustained discharge [39].

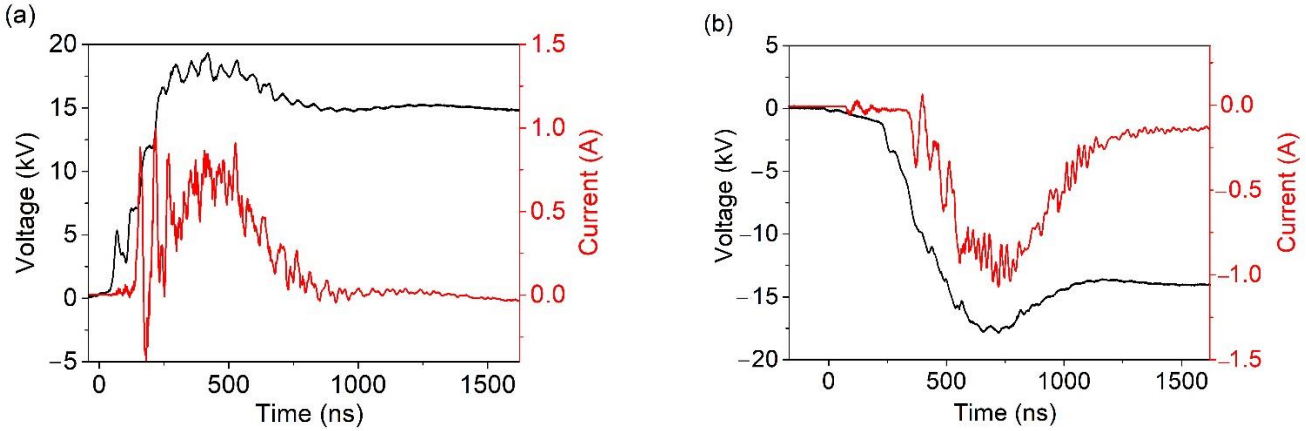

Figure 4. Typical discharge voltage and current waveforms for (**a**) positive pulse, and (**b**) negative pulse.

3.4. Gas Temperature of FEGLD

As a quantitative indicator, the gas temperature of FEGLD is acquired and discussed. Since the small energy gap between the rotational levels of the molecules, the translational–rotational equilibrium is readily achieved by frequent collisions between the heavy particles at AP [40]. The gas temperature can be considered approximately equal to the rotational temperature, and it can be acquired by analyzing the rotational spectra of excited molecular species [41,42]. In this work, the N_2 ($C^3\Pi_u \rightarrow B^3\Pi_g$, $\Delta\nu = -2$) is chosen to measure rotational temperature, because there is no overlap with OES emitting from He and other trace impurities originating from air, such as H and OH [43]. In this work, the *Specair* code [44] can be used to obtain the rotational temperature of N_2 ($C^3\Pi_u \rightarrow B^3\Pi_g$, $\Delta\nu = -2$) by comparing the simulated spectra and experimental spectra. As shown in Figure 5, under the experimental conditions of 3.5 L/min gas flow rate, 30 kV pulse peak voltage, and 12 mm discharge gap, the rotational temperature of N_2 ($C^3\Pi_u \rightarrow B^3\Pi_g$, $\Delta\nu = -2$) is 320 K, that is, close to the room temperature.

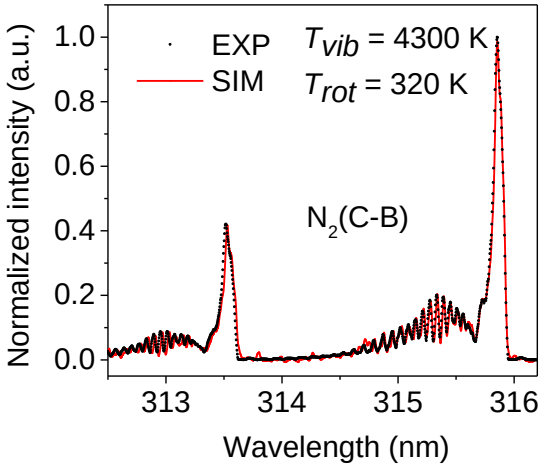

Figure 5. The measured and the best-fitting simulation spectra of N_2 ($C^3\Pi_u \rightarrow B^3\Pi_g$, $\Delta\nu = -2$).

3.5. Electron Density of FEGLD

The hydrogen line broadening effects of electron density on Stark broadening is one of the most widely used techniques for electron density measurement [45]. Both H_α and H_β could be used for the calculation. In this work, the H_α is preferred because of its high line shape sensitivity and adequate emission intensity. The emission line of H_α is the

convolution of the Gaussian and Lorentzian lines. The Gaussian profile was determined by both the Doppler and instrument broadening, in which the fullwidth at half maximum (FWHM) of the Gaussian is given by:

$$\Delta\lambda_G = (\Delta\lambda_D^2 + \Delta\lambda_I^2)^{\frac{1}{2}} \quad (1)$$

where $\Delta\lambda_D$ and $\Delta\lambda_I$ are the FWHM of the Doppler broadening and instrumental broadening, respectively.

Doppler broadening mainly depends on the temperature of the emitter [46]. The FWHM of the Doppler broadening is given by the expression [47]:

$$\Delta\lambda_D = 7.16 \times 10^{-7}\lambda(\frac{T_g}{M})^{\frac{1}{2}} \quad (2)$$

where λ is the emission wavelength, T_g is the gas temperature of plasma in K and M is the atomic weight of hydrogen atoms in g·mol^{-1}.

The broadening induced by the detection system is called apparatus function or instrumental broadening [41]. The instrument broadening in this work is determined by measuring the FWHM of the mercury lamp characteristic spectrum at 435.8 nm. Its value is given as:

$$\Delta\lambda_I = 0.078 \text{ nm} \quad (3)$$

while grating 1200 lines·mm^{-1} is used.

Lorentzian profiles are mainly determined by the Stark, van der Waals, resonance, and natural broadening, and the expression could be given by:

$$\Delta\lambda_L = \Delta\lambda_V + \Delta\lambda_S + \Delta\lambda_R + \Delta\lambda_N \quad (4)$$

Natural broadening is caused by the uncertainty principle of atomic stable state energy, and the expression could be given by:

$$\Delta E = \frac{h}{\Delta\lambda_N} = \frac{h}{2\pi\tau} \quad (5)$$

where ΔE is uncertainty of the energy level, h is Planck constant, τ is energy level lifetime in the order of 10^{-9}. The FWHM of natural broadening could be expressed as:

$$\Delta\lambda_N = 2\pi\tau \quad (6)$$

The value of natural line broadening is very small by calculation, in the orders of magnitude of 10^{-5} nm, which can be negligible in this study [48].

Resonance broadening occurs by electric dipole of the upper- or the lower-level transit to the ground state. The formula for the FWHM of resonance broadening could be written as follows [47,49]:

$$\Delta\lambda_R = 8.61 \times 10^{-30}\lambda^2\lambda_r f_r N_i(\frac{g_i}{g_k})^{\frac{1}{2}} \quad (7)$$

where λ is the wavelength of the spectral line, f_r is the absorption oscillator strength, which is 0.6407 when the transition is 2s–3p for H_α line [50], λ_r is the wavelength of the resonance line; g_k and g_i are the statistical weights of its upper and lower levels, which are 8 and 18, respectively [49]. N_i is the ground state number density. Since FEGLD operated in the open air with low H_2O concentration, the discharge happened on the liquid surface with low temperature, which is not enough to boil the water to improve the H_2O concentration highly. The resonance broadening should be out of consideration in this work.

Van der Waals broadening is generated by collisions of excited H atoms with another kind of species, which is the helium atom in this work. An approximate formula for the FWHM of it is [51]:

$$\Delta\lambda_V = 8.18 \times 10^{-26} \lambda_0^2 (\overline{R}^2)^{\frac{2}{5}} T_g^{\frac{3}{10}} N \sum_i \left(\frac{\alpha_i^{\frac{2}{5}} \chi_i}{\mu_i^{\frac{3}{10}}}\right) \quad (8)$$

where λ_0 is wavelength, μ is the reduced mass, N is the neutral particle density, i is He and χ the fraction of the perturber. Hofmann et al. [51] calculated and reported the experiential expressions of the van der Waals broadening for different gas compositions at atmospheric pressure, and the formula can be shown as follows, where the C can be given when discharge plasma operates with different work gases.

$$\Delta\lambda_V = \frac{C}{T_g^{\frac{7}{10}}} \quad (9)$$

In this work, the value of C is 2.42, which considers the plasma operating in air with helium as the work gas.

Stark broadening has high sensitivity to electron density. The relationship between the FWHM of the hydrogen alpha line and electron density is shown as follows [51]:

$$\Delta\lambda_S = 1.78 \times \left(\frac{n_e}{10^{23} m^{-3}}\right)^{\frac{2}{3}} \quad (10)$$

The line shapes of experimental and simulated H_α broadened by the above broadenings are shown in Figure 6. The values of FWHM for all the broadening mechanisms are presented in Table 2. The electron density is calculated to be about 2.2×10^{15} cm^{-3} under the conditions of 30 kV pulse peak voltage, 12 mm discharge gap, and 3.5 L/min gas flow rate.

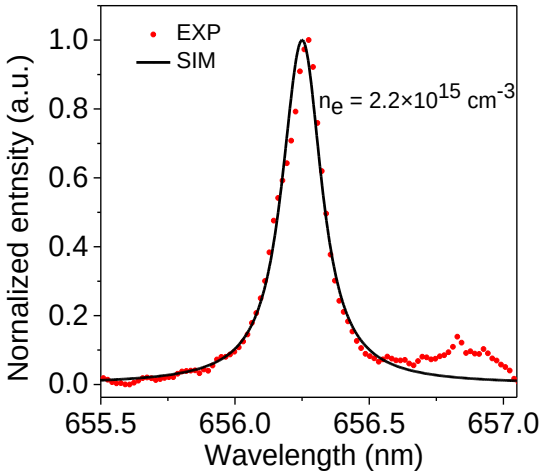

Figure 6. Comparison of the experimental H_α line and simulated line.

Table 2. Broadening of FEGLD plasma in H_α.

Broadening Effect	Value (nm)
Doppler broadening	0.008
Instrument broadening	0.078
Van der Waals broadening	0.044
Natural broadening	10^{-5}
Stark broadening	0.156

3.6. Spatial Distributions Characteristic of the FEGLD

For understanding the characteristic variation of discharge plasma in space, the spatially resolved emission intensity distributions of N_2 ($C^3\Pi_u \rightarrow B^3\Pi_g$), N_2^+ ($B^2\Sigma \rightarrow X^2\Pi$), OH ($A^2\Sigma \rightarrow X^2\Pi$), O ($3p^5P \rightarrow 3s^5S^0$), and He ($3s^3S \rightarrow 2p^3P^0$) of FEGLD are shown in Figure 7, under the experimental conditions of 12 mm discharge gap, 30 kV pulse peak voltage, and 3.5 L/min helium flow rate. In this part, the OES emitted from the different parts of FEGLD is obtained by optical fiber which is placed on the adjustable micrometer screw lifting platform.

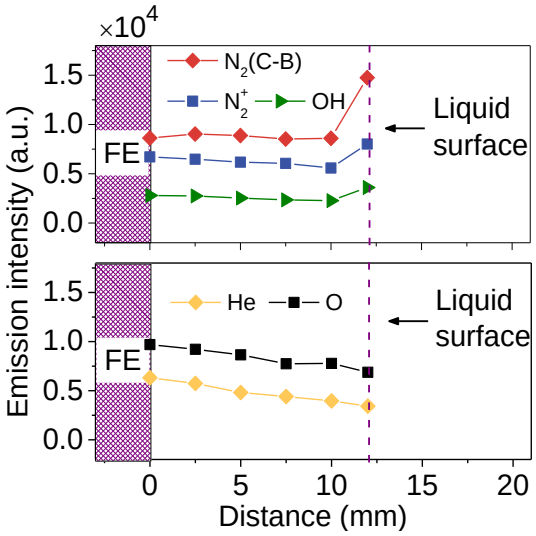

Figure 7. The spatial distributions of N_2 ($C^3\Pi_u \rightarrow B^3\Pi_g$), N_2^+ ($B^2\Sigma \rightarrow X^2\Pi$), OH ($A^2\Sigma \rightarrow X^2\Pi$), O ($3p^5P \rightarrow 3s^5S^0$) and He ($3s^3S \rightarrow 2p^3P^0$) emission intensities.

The inconsistent spatial distributions of FEGLD reactive species emission intensities along the axial direction can be found in Figure 7. In the range of 0–10 mm, the emission intensities of N_2 ($C^3\Pi_u \rightarrow B^3\Pi_g$), N_2^+ ($B^2\Sigma \rightarrow X^2\Pi$), and OH ($A^2\Sigma \rightarrow X^2\Pi$) remains constant. But in the range of 10–12 mm which is near to the liquid surface, the emission intensities of N_2^+ ($B^2\Sigma \rightarrow X^2\Pi$), N_2 ($C^3\Pi_u \rightarrow B^3\Pi_g$), and OH ($A^2\Sigma \rightarrow X^2\Pi$) show obvious increases and attain a peak value at 12 mm. Meanwhile, the emission intensities of He ($3s^3S \rightarrow 2p^3P^0$) and O ($3p^5P \rightarrow 3s^5S^0$) keep decreasing in the range of 0–12 mm. This is because there are differences in the excitation mechanism of radiative states. The formation of He ($3s^3S \rightarrow 2p^3P^0$) and N_2 ($C^3\Pi_u \rightarrow B^3\Pi_g$) is dominated by direct excitation by energetic electrons [52], which relies on the high electric field and the electron density. But near the liquid surface, there is no obvious increase in electron density which is clearly shown in Figure 8. According to the research in [53], a mushroom-like shape discharge area is generated due to the interaction with a liquid surface. The N_2 molecule from ambient air is involved in the discharge area. Thus, the emission intensity of N_2 ($C^3\Pi_u \rightarrow B^3\Pi_g$) increased here, and helium diffused here leading to the emission intensity of He ($3s^3S \rightarrow 2p^3P^0$) decreasing. The significant elevation of N_2^+ ($B^2\Sigma \rightarrow X^2\Pi$) emission intensity comes from the Penning process [52], in which the increase of nitrogen will induce the improvement of N_2^+ $(B^2\Sigma_u^+)_u$ generation. The formation of OH (A) via direct dissociative electron excitation of water or dissociative recombination of H_2O^+ or H_3O^+ [54] The increase of OH ($A^2\Sigma \rightarrow X^2\Pi$) emission intensity near the liquid surface is also shown in [52]. The H_2O^+(A) ion could exist in a mushroom-like shape area due to its relatively long radiative lifetime (about 10 μs), so the increase of OH ($A^2\Sigma \rightarrow X^2\Pi$) emission intensity can be observed near the liquid surface.

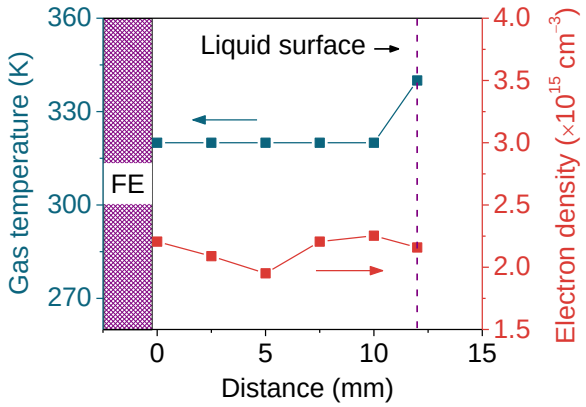

Figure 8. Gas temperature and electron density distribution in the axial direction.

As the important parameters, gas temperature and electron density influence the gas–liquid discharge application. The spatially resolved gas temperature and electron density of FEGLD are shown in Figure 8 when the pulse peak voltage, gas flow rate, and discharge gap are kept at 30 kV, 3.5 L/min, and 12 mm, respectively. It clearly shows that the electron density remains at 2.2×10^{15} cm^{-3}, almost without changes in the axial direction. The gas temperature remains at 320 K in the range of 1–12 mm, and reaches maxima of 340 K at 12 mm which is near the liquid surface. The increase in gas temperature near the liquid is also shown by Verreycken et al. [55] who attributed it to the fast vibration-to-vibration (V–V) process of O_2–H_2O and N_2–H_2O and, at the same time, H_2O's higher vibration-to-translation (V–T) rate compared to O_2 and N_2, which means that as the H_2O concentration increases, additional gas heating occurs. One et al. [56] found that the temperature will be elevated while water vapor concentration increases. Moreover, since the inelastic collisions between electrons and heavy particles induce the plasma chemistry [57], which could be have potential applications in the treatment of living human and animal tissue [58], for instance, the high electron density plasma with approximately room temperature at AP is expected to meet temperature-sensitive needs.

3.7. The Effects of Discharge Gap on FEGLD

Considering the space compatibility during actual operation, the effect of the discharge gap on active species, the gas temperature, and the electron density are discussed. Figure 9 shows the effects of the discharge gap on the emission intensities of N_2 ($C^3\Pi_u \rightarrow B^3\Pi_g$), N_2^+ ($B^2\Sigma \rightarrow X^2\Pi$), OH ($A^2\Sigma \rightarrow X^2\Pi$), O ($3p^5P \rightarrow 3s^5S^0$), and He ($3s^3S \rightarrow 2p^3P^0$) of the FEGLD under the measurement condition of 30 kV plus peak voltage and 3.5 L/min gas flow rate. It clearly shows that the emission intensities of N_2 ($C^3\Pi_u \rightarrow B^3\Pi_g$), N_2^+ ($B^2\Sigma \rightarrow X^2\Pi$), OH ($A^2\Sigma \rightarrow X^2\Pi$), and O ($3p^5P \rightarrow 3s^5S^0$) remain almost constant as the discharge gap is enlarged from 10 mm to 15 mm. But in the same conditions, the emission intensity of He ($3s^3S \rightarrow 2p^3P^0$) decreases while the discharge gap changes from 10 mm to 13 mm. Since the emission spectrum of He ($3s^3S \rightarrow 2p^3P^0$) is an indicator of energetic electrons with relatively high threshold energy of 22.7 eV [59], the decrease of emission intensity of He ($3s^3S \rightarrow 2p^3P^0$) reflects the change in electron energy distribution, which is controlled by the applied reduced field E/N [60]. As the discharge gap is enlarged, the increase in the value of pressure multiplied by electrode gap distance led to the fall in the reduced electric field, which induces the energy of electrons to decrease [61], and then the emission intensity of He ($3s^3S \rightarrow 2p^3P^0$) is obviously decreased here.

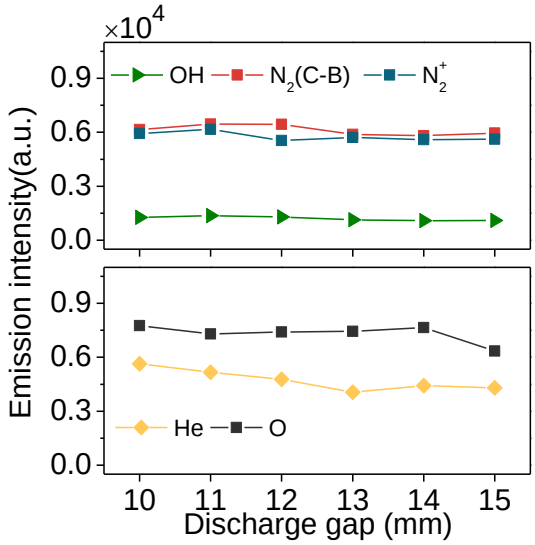

Figure 9. Effects of the discharge gap on the emission intensities of N_2 ($C^3\Pi_u \rightarrow B^3\Pi_g$), N_2^+ ($B^2\Sigma \rightarrow X^2\Pi$), OH ($A^2\Sigma \rightarrow X^2\Pi$), O ($3p^5P \rightarrow 3s^5S^0$), and He ($3s^3S \rightarrow 2p^3P^0$).

The effects of the discharge gap on gas temperature and electron density of FEGLD are illustrated in Figure 10 under the measurement conditions of 30 kV plus peak voltage and 3.5 L/min gas flow rate. As shown in the figure, the electron density shows almost no change as the discharge gap increases. However, the gas temperature increased from 280 K to 350 K with the discharge gap elevated from 10 mm to 14 mm. Since the optical fiber is aimed at the medium area of FEGLD, it means this increase in gas temperature happened in the middle of the discharge plasma. Considering Figure 2, which shows clearly that the diameter of the discharge area near the liquid surface decreased with the discharge gap enlarging, the mushroom-like shape discharge, which is around the mean middle discharge, is not obvious. Therefore, the cooling effect is limited, which is expressly significant for the helium gas with high thermal conductivity at 1.6×10^3 J cm^{-1} s^{-1} K^{-1}. Hence, in this work, the weakness of the cooling effect around the middle discharge area leads to the increase in gas temperature.

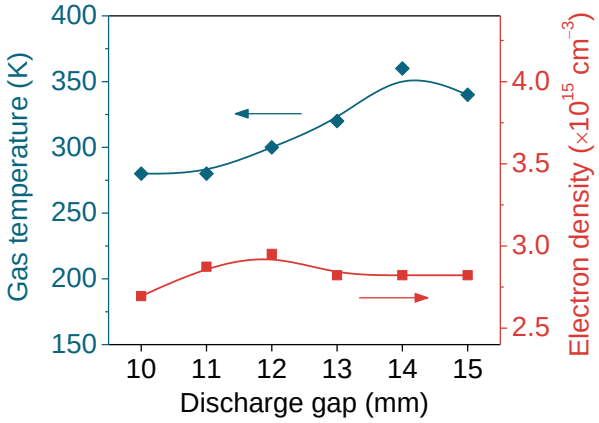

Figure 10. Effects of the discharge gap on gas temperature and electron density.

3.8. The Effects of the Helium Flow Rate on FEGLD

Since the gas flow rate influences the time for gas stay, it further affects temperature transition and discharge characteristics. The effect of helium flow rate on the emission intensity of N_2 ($C^3\Pi_u \rightarrow B^3\Pi_g$), N_2^+ ($B^2\Sigma \rightarrow X^2\Pi$), OH ($A^2\Sigma \rightarrow X^2\Pi$), O ($3p^5P \rightarrow 3s^5S^0$), and He ($3s^3S \rightarrow 2p^3P^0$) are obtained and shown in Figure 11, under the experimental conditions of 12 mm discharge gap and 30 kV pulse peak voltage. It can be seen that as the

gas flow rate is turned up, the emission intensities of N_2^+ ($B^2\Sigma \rightarrow X^2\Pi$), He ($3s^3S \rightarrow 2p^3P^0$), and O ($3p^5P \rightarrow 3s^5S^0$) increased gradually. Meanwhile, the reduction in emission intensity of N_2 ($C^3\Pi_u \rightarrow B^3\Pi_g$) and OH ($A^2\Sigma \rightarrow X^2\Pi$) can be observed. In the study by Yue et al. [62], OH distribution with different gas flow rates is reported. As the gas flow rate is increased, the OH distribution trends to uniform; meanwhile, the peak intensity value of OH-LIF is getting weaker. The influence of gas flow rate on O-LIF is also reported; it is due to the O ($3p^5P$) having generated a relatively long lifetime of up to milliseconds [63] that the distribution of atoms could be influenced by gas flow. Similarly, as discussed before, the emission intensity of N_2^+ ($B^2\Sigma \rightarrow X^2\Pi$) is dominated by the Penning process, and the metastable helium with long lifetime is driven by gas flow in the FEGLD, which leads to emission intensities of N_2^+ ($B^2\Sigma \rightarrow X^2\Pi$) increasing.

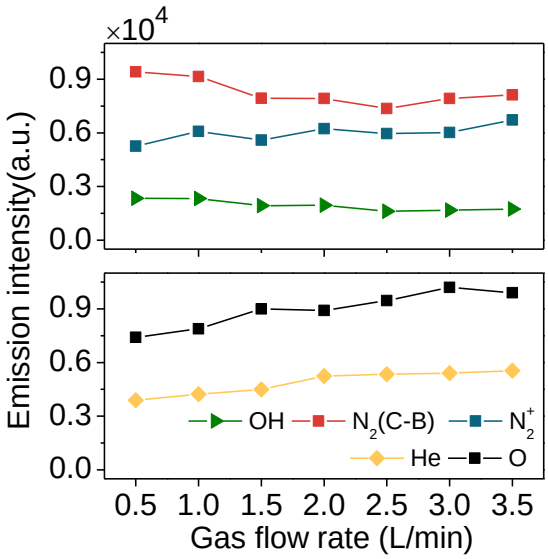

Figure 11. Effects of helium flow rate on the emission intensity of N_2 ($C^3\Pi_u \rightarrow B^3\Pi_g$), N_2^+ ($B^2\Sigma \rightarrow X^2\Pi$), OH ($A^2\Sigma \rightarrow X^2\Pi$), O ($3p^5P \rightarrow 3s^5S^0$), and He ($3s^3S \rightarrow 2p^3P^0$).

The effects of gas flow rate on gas temperature and electron density are illustrated in Figure 12, where the pulse peak voltage and discharge gap are kept at 30 kV and 12 mm, respectively. It clearly shows that the gas temperature of FEGLD almost remains at 330 ± 10 K when the gas flow rate varied from 0.5 L/min to 3.5 L/min, suggesting that the FEGLD has good stability. The electron density increases obviously from 2.3×10^{15} cm^{-3} to 2.7×10^{15} cm^{-3}, while the helium gas flow rate increased from 0.5 L/min to 3.5 L/min, which is the most obvious consistent improvement in this work. Since gas flow could promote collision processes [34], the reactions that could generate electrons are highly promoted by the increase in the gas flow rate. Meanwhile, the increase in high energy metastable helium amount is beneficial to generating the Penning process, which provides seed electrons for discharge. As the results show, increasing the gas flow can avoid gas heating and at the same time improve electron density and the capacity that generates reactive species such as O, which is one of the most important active species in plasma medicine applications [52]. This shows the potential for meeting the needs of such temperature-sensitive applications.

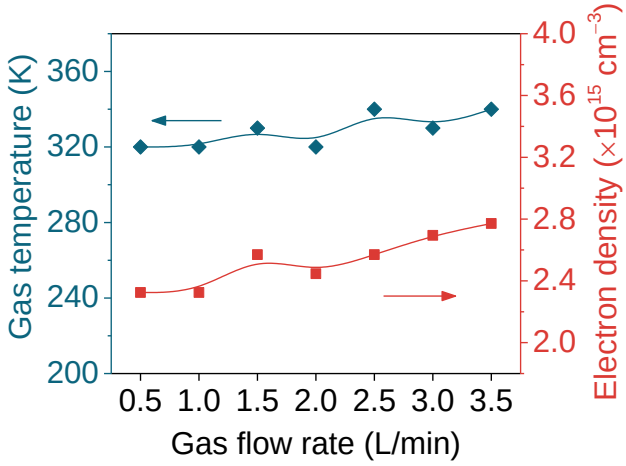

Figure 12. Effects of gas flow rate on gas temperature and electron density.

4. Conclusions

In this paper, combined with nanosecond pulse voltage and a floating electrode, a stable gas–liquid discharge with electron density of 2.3 × 10^{15} cm^{-3} and low gas temperature of 320 K ± 20 K is obtained at AP. The OES spatial distributions show that gas temperature and emission intensities of N_2 ($C^3\Pi_u \rightarrow B^3\Pi_g$), N_2^+ ($B^2\Sigma \rightarrow X^2\Pi$), and OH ($A^2\Sigma \rightarrow X^2\Pi$) increase noticeably near the liquid surface. A large discharge area of 20 mm diameter is generated over the liquid surface when the discharge gap is set at 10 mm. As the discharge gap is increased further, obvious contraction is clearly shown in this area, with emission intensities of reactive species and electron density remaining constant. However, the electron density and emission intensity of reactive species such as O can be elevated by turning up the gas flow rate, whereas no obvious gas heating is observed.

Author Contributions: Investigation, M.Z.; Project administration, D.Y.; Supervision, Y.L. (Yunhu Liu), H.Y., J.L., Y.L. (Yao Li) and D.Y.; Writing—original draft, S.L.; Writing—review & editing, J.L. and D.Y. All authors have read and agreed to the published version of the manuscript.

Funding: This research was funded by [National Natural Science Foundations of China] grant number [11965018, 51977023 and 52077026], [Science and Technology Development Fund of Xinjiang Production and Construction] grant number [2019BC009], [Fundamental Research Funds for the Central Universities] grant number [DUT21LK31], [Key Laboratory Fund of National Defense Science and Technology] grant number [6142605200303], [Science and Technology Plan Project of the Ninth Division of the Crops] grant number [2021JS003].

Conflicts of Interest: The authors declare no conflict of interest.

References

1. El Shaer, M.; Eldaly, M.; Heikal, G. Antibiotics Degradation and Bacteria Inactivation in Water by Cold Atmospheric Plasma Discharges Above and Below Water Surface. *Plasma Chem. Plasma Process.* **2020**, *40*, 971–983. [CrossRef]
2. Gururani, P.; Bhatnagar, P.; Bisht, B. Cold plasma technology: Advanced and sustainable approach for wastewater treatment. *Environ. Sci. Pollut. Res. Int.* **2021**, *28*, 65062–65082. [CrossRef] [PubMed]
3. Yang, D.Z.; Zhou, X.F.; Liang, J.P. Degradation of methylene blue in liquid using high-voltage pulsed discharge plasma synergizing iron-based catalyst-activated persulfate. *J. Phys. D Appl. Phys.* **2021**, *54*, 244002. [CrossRef]
4. Laroussi, M.; Bekeschus, S.; Keidar, M. Low-Temperature Plasma for Biology, Hygiene, and Medicine: Perspective and Roadmap. *IEEE Trans. Radiat. Plasma Med. Sci.* **2022**, *6*, 127–157. [CrossRef]
5. Qin, H.; Qiu, H.; He, S.T. Efficient disinfection of SARS-CoV-2-like coronavirus, pseudotyped SARS-CoV-2 and other coronaviruses using cold plasma induces spike protein damage. *J. Hazard. Mater.* **2022**, *430*, 128414. [CrossRef] [PubMed]
6. Busco, G.; Robert, E.; Chettouh-Hammas, N. The emerging potential of cold atmospheric plasma in skin biology. *Free Radic. Biol. Med.* **2020**, *161*, 290–304. [CrossRef]
7. Lu, Q.F.; Li, J.L.; Yu, J. Preparation of Ta_2O_5 nanoparticles by using cathode glow discharge electrolysis. *Mater. Res. Express.* **2021**, *8*, 125011. [CrossRef]

8. Sirotkin, N.A.; Khlyustova, A.V.; Titov, V.A. The Use of a Novel Three-Electrode Impulse Underwater Discharge for the Synthesis of W-Mo Mixed Oxide Nanocomposites. *Plasma Chem. Plasma Process.* **2021**, *42*, 191–209. [CrossRef]
9. Wang, H.; Xu, Q.; Zhou, X. Highly efficient adsorptive removal of persistent organic pollutants using NPD-acid combined modified NaY zeolites. *Chem. Eng. J.* **2022**, *431*, 133858. [CrossRef]
10. Liu, W.; Bao, Y.; Duan, X. Study on water treatment effect of dispersion discharge plasma based on flowing water film electrode. *Plasma Sci. Technol.* **2021**, *23*, 105502. [CrossRef]
11. Zhou, R.; Liu, B.; Li, Y. Reduced breakdown voltage for in-liquid plasma discharges using moveable electrodes. *J. Phys. D Appl. Phys.* **2021**, *55*, 10LT01. [CrossRef]
12. Liang, J.; Zhou, X.; Zhao, Z. Discharge characteristics and reactive species production of unipolar and bipolar nanosecond pulsed gas–liquid discharge generated in atmospheric N_2. *Plasma Sci. Technol.* **2021**, *23*, 095405. [CrossRef]
13. Szulc, M.; Forster, G.; Marques-Lopez, J.L. Influence of Pulse Amplitude and Frequency on Plasma Properties of a Pulsed Low-Current High-Voltage Discharge Operated at Atmospheric Pressure. *Appl. Sci.* **2022**, *12*, 6580. [CrossRef]
14. Liang, J.; Zhou, X.; Zhao, Z. Reactive oxygen and nitrogen species in Ar + N_2 + O_2 atmospheric-pressure nanosecond pulsed plasmas in contact with liquid. *Phys. Plasmas* **2019**, *26*, 023521. [CrossRef]
15. Korolev, Y.D.; Frants, O.B.; Landl, N.V. Features of a near-cathode region in a gliding arc discharge in air flow. *Plasma Sources Sci. Technol.* **2014**, *23*, 54016. [CrossRef]
16. Baeva, M.; Loffhagen, D.; Becker, M.M. Fluid Modelling of DC Argon Microplasmas: Effects of the Electron Transport Description. *Plasma Chem. Plasma Process.* **2019**, *39*, 949–968. [CrossRef]
17. Rousso, A.C.; Goldberg, B.M.; Chen, T.Y. Time and space resolved diagnostics for plasma thermal-chemical instability of fuel oxidation in nanosecond plasma discharges. *Plasma Sources Sci. Technol.* **2020**, *29*, 105012. [CrossRef]
18. Saifutdinov, A.I. Unified simulation of different modes in atmospheric pressure DC discharges in nitrogen. *J. Appl. Phys.* **2021**, *129*, 093302. [CrossRef]
19. Bruggeman, P.J.; Iza, F.; Brandenburg, R. Foundations of atmospheric pressure non-equilibrium plasmas. *Plasma Sources Sci. Technol.* **2017**, *26*, 123002. [CrossRef]
20. Bruggeman, P.J.; Frontiera, R.R.; Kortshagen, U.R. Plasma-driven solution electrolysis. *J. Appl. Phys.* **2021**, *129*, 200902. [CrossRef]
21. Yang, D.Z.; Jia, L.; Wang, W.C. Atmospheric Pressure Gas-Liquid Diffuse Nanosecond Pulse Discharge Used for Sterilization in Sewage. *Plasma Process Polym.* **2014**, *11*, 842–849. [CrossRef]
22. Yuan, H.; Yang, D.; Jia, Z. Activated Carbon Modified by Nanosecond Pulsed Discharge for Polycyclic Aromatic Hydrocarbons Detection. *Plasma Chem. Plasma Process.* **2020**, *40*, 1539–1553. [CrossRef]
23. Herrmann, A.; Margot, J.; Hamdan, A. Influence of voltage and gap distance on the dynamics of the ionization front, plasma dots, produced by nanosecond pulsed discharges at water surface. *Plasma Sources Sci. Technol.* **2022**, *31*, 045006. [CrossRef]
24. Gromov, M.; Leonova, K.; Britun, N. Plasma nitrogen fixation in the presence of a liquid interface: Role of OH radicals. *React. Chem. Eng.* **2022**, *7*, 1047–1052. [CrossRef]
25. Xu, H.; Liu, D.; Xia, W. Comparison between the water activation effects by pulsed and sinusoidal helium plasma jets. *Phys. Plasmas* **2018**, *25*, 013520. [CrossRef]
26. Wang, S.; Yang, D.; Liu, F. Spectroscopic study of bipolar nanosecond pulse gas-liquid discharge in atmospheric argon. *Plasma Sci. Technol.* **2018**, *20*, 075404. [CrossRef]
27. Wang, S.; Yang, D.Z.; Zhou, R. Mode transition and plasma characteristics of nanosecond pulse gas–liquid discharge: Effect of grounding configuration. *Plasma Process Polym.* **2019**, *17*, 1900146. [CrossRef]
28. Divya Deepak, G. Review on recent advances in cold plasma technology. *Eur. Phys. J. Appl. Phys.* **2022**, *97*, 39. [CrossRef]
29. Zhu, T.; Liu, J.; Xin, Y. Hydrogen production by microwave discharge in liquid: Study on the characteristics effect of suspended electrode. *J. Anal. Appl. Pyrolysis* **2022**, *164*, 164. [CrossRef]
30. Hu, W.; Wang, J.; Xu, W. Electrical and Optical Characteristics of a Color Alternating Current Plasma Display Panel With Floating Electrodes. *J. Disp. Technol.* **2013**, *9*, 100–105. [CrossRef]
31. Lee, H.W.; Nam, S.H.; Mohamed, A.-A.H. Atmospheric Pressure Plasma Jet Composed of Three Electrodes: Application to Tooth Bleaching. *Plasma Process Polym.* **2010**, *7*, 274–280. [CrossRef]
32. Liu, W.; Ma, C.; Li, Z. Generation of atmospheric-pressure homogeneous dielectric barrier discharge in air. *EPL Europhys. Lett.* **2017**, *118*, 45001. [CrossRef]
33. Liu, Z.J.; Wang, W.C.; Zhang, S. Optical study of a diffuse bipolar nanosecond pulsed dielectric barrier discharge with different dielectric thicknesses in air. *Eur. Phys. J. D* **2012**, *66*, 319. [CrossRef]
34. Eichwal, O. Coupling of chemical kinetics, gas dynamics, and charged particle kinetics models for the analysis of NO reduction from flue gases. *J. Appl. Phycol.* **1997**, *82*, 4781–4794. [CrossRef]
35. Yang, D.; Wang, W.; Wang, K. Spatially resolved spectra of excited particles in homogeneous dielectric barrier discharge in helium at atmospheric pressure. *Spectrochim. Acta A* **2010**, *76*, 224–229. [CrossRef]
36. Niemi, K.; Waskoenig, J.; Sadeghi, N. The role of helium metastable states in radio-frequency driven helium–oxygen atmospheric pressure plasma jets: Measurement and numerical simulation. *Plasma Sources Sci. Technol.* **2011**, *20*, 055005. [CrossRef]
37. Liu, Y.; Liu, D.; Zhang, J. 1D fluid model of RF-excited cold atmospheric plasmas in helium with air gas impurities. *Phys. Plasmas* **2020**, *27*, 043512. [CrossRef]

38. Kovačević, V.V.; Dojčinović, B.P.; Jović, M. Measurement of reactive species generated by dielectric barrier discharge in direct contact with water in different atmospheres. *J. Phys. D Appl. Phys.* **2017**, *50*, 155205. [CrossRef]
39. Lai, J.; Foster, J.E. Time-resolved imaging of streamer formation inside gaseous bubbles in liquids. *J. Phys. D Appl. Phys.* **2020**, *53*, 025206. [CrossRef]
40. Luo, S.; Denning, C.M.; Scharer, J.E. Laser-rf creation and diagnostics of seeded atmospheric pressure air and nitrogen plasmas. *J. Appl. Phys.* **2008**, *104*, 013301. [CrossRef]
41. Bruggeman, P.J.; Sadeghi, N.; Schram, D.C. Gas temperature determination from rotational lines in non-equilibrium plasmas: A review. *Plasma Sources Sci. Technol.* **2014**, *23*, 023001. [CrossRef]
42. Zhang, L.; Yang, D.; Wang, W. Needle-array to Plate DBD Plasma Using Sine AC and Nanosecond Pulse Excitations for Purpose of Improving Indoor Air Quality. *Sci. Rep.* **2016**, *6*, 25242. [CrossRef] [PubMed]
43. Wang, Q.; Koleva, I.; Donnelly, V.M. Spatially resolved diagnostics of an atmospheric pressure direct current helium microplasma. *J. Phys. D Appl. Phys.* **2005**, *38*, 1690–1697. [CrossRef]
44. Laux, C.O. Optical diagnostics of atmospheric pressure air plasmas. *Plasma Sources Sci. Technol.* **2003**, *12*, 125–138. [CrossRef]
45. Nikiforov, A.Y.; Leys, C.; Gonzalez, M.A. Electron density measurement in atmospheric pressure plasma jets: Stark broadening of hydrogenated and non-hydrogenated lines. *Plasma Sources Sci. Technol.* **2015**, *24*, 015015. [CrossRef]
46. Gigosos, M.A.; González, M.Á.; Cardeñoso, V.n. Computer simulated Balmer-alpha, -beta and -gamma Stark line profiles for non-equilibrium plasmas diagnostics. *Sci. Rep.* **2003**, *58*, 1489–1504. [CrossRef]
47. Djurović, S.; Konjević, N. On the use of non-hydrogenic spectral lines for low electron density and high pressure plasma diagnostics. *Plasma Sources Sci. Technol.* **2009**, *18*, 035011. [CrossRef]
48. Qian, M.; Ren, C.; Wang, D. Stark broadening measurement of the electron density in an atmospheric pressure argon plasma jet with double-power electrodes. *J. Appl. Phys.* **2010**, *107*, 063303. [CrossRef]
49. Adams, N.G.; Bhatia, A.K.; Amusia, M.Y.; Louck, D.J.; Jud, R.B.; Paldus, J.; Hill, N.R.; Gallagher, A.; Fischer, F.C.; Grant, P.I.; et al. *Springer Hand Book of Atomic Molecular, and Optical Physics*; Drake, G.W.F., Ed.; Drake Springer Science+Business Media, Inc.: New York, NY, USA, 2006; ISBN 978-3-030-73892-1.
50. Cox, A.N.; Däppen, W.; Cowley, C.; Wiese, L.W.; Fuhr, J.; Kuznetsova, A.L.; Keady, J.J.; Kilcrease, D.P.; Hjellming, M.R.; Tokunaga, A.T.; et al. *Allen Astrophysical Quantities*; Springer: New York, NY, USA, 1999; ISBN 978-1-4612-1186-0.
51. Hofmann, S.; van Gessel, A.F.H.; Verreycken, T. Power dissipation, gas temperatures and electron densities of cold atmospheric pressure helium and argon RF plasma jets. *Plasma Sources Sci. Technol.* **2011**, *20*, 065. [CrossRef]
52. Sretenovic, G.B.; Krstic, I.B.; Kovacevic, V.V. Spectroscopic Study of Low-Frequency Helium DBD Plasma Jet. *IEEE Trans. Plasma Sci.* **2012**, *40*, 2870–2878. [CrossRef]
53. Kovačević, V.V.; Sretenović, G.B.; Slikboer, E. The effect of liquid target on a nonthermal plasma jet—imaging, electric fields visualization of gas flow and optical emission spectroscopy. *J. Phys. D Appl. Phys.* **2018**, *51*, 065202. [CrossRef]
54. Bruggeman, P.; Iza, F.; Guns, P. Electronic quenching of OH(A) by water in atmospheric pressure plasmas and its influence on the gas temperature determination by OH(A–X) emission. *Plasma Sources Sci. Technol.* **2010**, *19*, 015016. [CrossRef]
55. Verreycken, T.; van Gessel, A.F.H.; Pageau, A. Validation of gas temperature measurements by OES in an atmospheric air glow discharge with water electrode using Rayleigh scattering. *Plasma Sources Sci. Technol.* **2011**, *20*, 024002. [CrossRef]
56. Ono, R.; Teramoto, Y.; Oda, T. Effect of humidity on gas temperature in the afterglow of pulsed positive corona discharge. *Plasma Sources Sci. Technol.* **2010**, *19*, 015009. [CrossRef]
57. Tendero, C.; Tixier, C.; Tristant, P. Atmospheric pressure plasmas: A review. *Sci. Rep.* **2006**, *61*, 2–30. [CrossRef]
58. Fridman, G.; Peddinghaus, M.; Balasubramanian, M. Blood Coagulation and Living Tissue Sterilization by Floating-Electrode Dielectric Barrier Discharge in Air. *Plasma Chem. Plasma Process.* **2006**, *26*, 425–442. [CrossRef]
59. Walsh, J.L.; Iza, F.; Janson, N.B. Three distinct modes in a cold atmospheric pressure plasma jet. *J. Phys. D Appl. Phys.* **2010**, *43*, 075201. [CrossRef]
60. Lepikhin, N.D.; Luggenhölscher, D.; Czarnetzki, U. Electric field measurements in a He:N2 nanosecond pulsed discharge with sub-ns time resolution. *J. Phys. D Appl. Phys.* **2021**, *54*, 055201. [CrossRef]
61. Wang, S.; Wang, W.C.; Yang, D.Z. Optical and application study of gas-liquid discharge excited by bipolar nanosecond pulse in atmospheric air. *Spectrochim. Acta A* **2014**, *131*, 571–576. [CrossRef] [PubMed]
62. Yue, Y.; Pei, X.; Gidon, D. Investigation of plasma dynamics and spatially varying O and OH concentrations in atmospheric pressure plasma jets impinging on glass, water and metal substrates. *Plasma Sources Sci. Technol.* **2018**, *27*, 064001. [CrossRef]
63. Iseki, S.; Ohta, T.; Aomatsu, A. Rapid inactivation of Penicillium digitatum spores using high-density nonequilibrium atmospheric pressure plasma. *Appl. Phys. Lett.* **2010**, *96*, 153704. [CrossRef] [PubMed]